



1 **Sea Surface Temperature over the Bay of Bengal: A key**
2 **driver for South Asian Summer Monsoon rainfall during past**
3 **31 kiloyears**

4 Thamizharasan Sakthivel^{1,2}, Prosenjit Ghosh^{1,2}, Ravi Bhushan³, Harsh Raj³, Ankur J Dabhi³,
5 Ajay Shivam³, Senthilnathan D⁴

6 ¹Centre for Earth Sciences, Indian Institute of Science, Bangalore, India 560012.

7 ²Divecha Centre for Climate Change, Indian Institute of Science, Bangalore, India 560012.

8 ³Geosciences Division, Physical Research Laboratory, Ahmedabad, India 380009.

9 ⁴Department of Earth Sciences, Pondicherry University, Puducherry, India 605014.

10 *Correspondence to:* Prosenjit Ghosh (pghosh@iisc.ac.in)

11 **Abstract:**

12 Warmer Sea Surface Temperature (SST) in the Bay of Bengal (BoB) is crucial for driving deep
13 atmospheric convection, facilitating low-level south-westerly winds, and enhancing moisture
14 transport, thereby intensifying South Asian Summer Monsoon (SASM) rainfall over South
15 Asia. However, the specific impact of BoB SST on SASM rainfall during the Glacial-
16 Interglacial periods remains poorly understood. In this study, we reconstructed SST and
17 evaporation versus rainfall variability over the past 31 kiloyears by simultaneously analyzing
18 the carbonate clumped isotopes and stable oxygen isotopic composition of surface-dwelling
19 planktic foraminifera *Globigerinoides ruber* from the Central West BoB (CWBoB), a key
20 moisture source region. Additionally, cloud cover index was inferred from the abundance ratio
21 of planktic foraminifera *Globigerina bulloides* to *Neogloboquadrina dutertrei*. Our SST
22 reconstruction reveals an 8°C variability over the past 31 kyr, coinciding with shifts in the *G.*
23 *bulloides* to *N. dutertrei* ratio during the Last Glacial period and deglaciation, suggesting SST
24 regulation by variable cloud cover. The increase in SST from the Early Holocene is attributed



25 to CO₂ radiative forcing. The stable oxygen isotope of seawater $\delta^{18}\text{O}_{\text{sw}}$ strongly aligns with a
26 proxy record of SASM wind intensity, indicating that changes in wind patterns drive the
27 variable evaporation versus rainfall dynamics over CWBoB. Furthermore, we examined the
28 temporal variation in SASM continental runoff and rainfall to the Northern BoB (NBoB) by
29 assessing changes in $\delta^{18}\text{O}_{\text{sw}}$ ($\Delta^{18}\text{O}_{\text{sw}}$), a proxy for Sea Surface Salinity (ΔSSS), between the
30 NBoB and CWBoB. Our analysis revealed a significant relationship between SASM rainfall
31 and SST in the CWBoB, indicating a sensitivity of 0.9 ± 0.1 psu drop in ΔSSS across the NBoB
32 per 1°C rise in SST. These findings enhance our understanding of the relationship between
33 CWBoB SST and SASM rainfall, highlighting the intricate dynamics of monsoon variability
34 and paving the way for improved predictability of SASM rainfall patterns.

35 **1. Introduction:**

36 Bay of Bengal (BoB) contributes 45-75% of total moisture to South Asian Summer Monsoon
37 (SASM) rainfall (Dar and Ghosh, 2016; Yoon and Chen, 2005), which accounts for 78% of
38 annual rainfall in the region (Parthasarathy et al., 1994). Variability in SASM rainfall
39 significantly affects economic growth for populations hosted in South Asian countries (Gadgil
40 and Gadgil, 2006). This highlights the significance of SASM rainfall variability as a crucial yet
41 uncertain factor in regional climatology. The thermodynamic conditions of seas surrounding
42 the continent have an important role in the future variability of SASM rainfall (Sein et al.,
43 2024; Sharma et al., 2023; Dinezio et al., 2020). The optimal sea surface temperatures (SST)
44 in the BoB, exceeding the range of 26-28°C, act as a threshold for initiating and sustaining the
45 process of deep atmospheric convection (Shenoi, 2002). This contributes to increased upper-
46 tropospheric temperatures, driving low-level winds from the south-west direction. These winds
47 integrate regional moisture, leading to the intensification of SASM rainfall (Goswami, 1987;
48 Hurley and Boos, 2015; Shenoi, 2002; Samanta et al., 2018). Any decrease in SST over the
49 BoB during summer is associated with the failure of the SASM (Vecchi and Harrison, 2002).



50 Even the inaccurate simulation of BoB SST in forecast climate models introduces bias in
51 SASM rainfall predictions (Samanta et al., 2018). However, despite this thermodynamic
52 understanding, the relationship between BoB SST and SASM rainfall is disrupted in the
53 instrumental age record due to the interplay of short-term climate phenomena such as El Niño-
54 Southern Oscillation, the Indian Ocean Dipole, and the North Atlantic cooling (Goswami et al.,
55 2022; Saxena and Pandey, 2021). These phenomena influence global oceanic and atmospheric
56 processes, including the moisture transport process over the Bay of Bengal (Chakraborty and
57 Singhai, 2021; Borah et al., 2020). The long-time-integrated record reduces interference from
58 transient climatic phenomena described above (Wang et al., 2017), offering invaluable insight
59 into the sensitivity of climatological BoB SST to SASM rainfall variability.

60 The Last Glacial and Holocene periods offer a valuable time window for estimating the role of
61 BoB SST on regional moisture transport. This time frame appropriately represents a significant
62 change in atmospheric CO₂ concentrations, ranging between 180 and 280 ppm (Bereiter et al.,
63 2015). Additionally, there is a difference in summer solar insolation values between 30°N and
64 the equator, varying between 84 W/m² and 102 W/m² (Berger, 1992). These variations
65 contribute to land-sea thermal and pressure contrasts, which in turn affect SASM wind strength
66 and rainfall distribution (Goswami et al., 1999; Webster, 1994; Rajeev et al., 2012; Evans et
67 al., 2015). Also, a geographic configuration similar to modern-day one serves as a template for
68 validating climate model predictions with variable SST conditions globally and over the BoB
69 region (Tierney et al., 2020; DiNezio et al., 2018). The role of BoB SST in influencing SASM
70 intensity has been addressed in a limited number of studies. These studies utilize proxies, such
71 as the stable hydrogen isotopic composition of leaf wax (δD) and the Ba/Ca ratio in planktic
72 foraminifera *G. ruber* from sediment cores in the Northern BoB (NBoB), to qualitatively
73 understand SASM rainfall variability (Wang et al., 2022; Weldeab et al., 2022). Here, the
74 authors compromised with the susceptibility of the isotopic signature preserved in δD of leaf

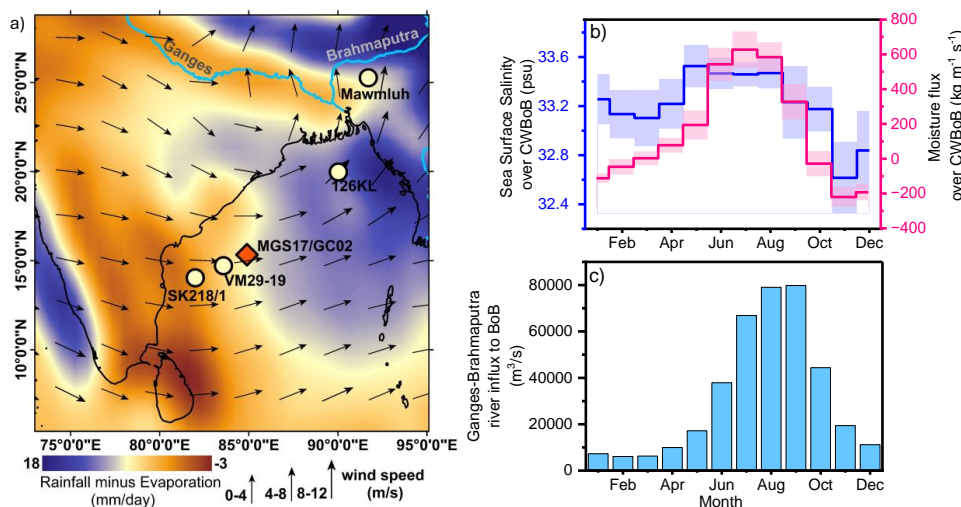


75 wax to deduce rainfall amount due to the interplay of factors such as the isotopic signature of
76 a moisture source, moisture recycling, and isotopic fractionation associated with shifts in
77 vegetational type (Sachse et al., 2012). The parameter Ba/Ca in *G. ruber* is interpreted as a
78 proxy for Sea Surface Salinity (SSS), assuming that riverine input is the primary driver for SSS
79 (Weldeab et al., 2022). However, this assumption is often invalidated by processes such as
80 evaporation or rainfall occurring within a sea or ocean (Hönisch et al., 2011).

81 Here, we retrieved a 4.3 m gravity core (MGS17/GC02) at the coordinates 15°19'36" N,
82 84°54'03" E, at a water depth of 2986m, situated within the Central West Bay of Bengal
83 (CWBoB) region (Fig. 1a). The sedimentary succession consists of dark grey and grey layer
84 with variable organic content and their primary constituents are hemipelagic clay with
85 calcareous foraminifera and nannofossils. The calcareous sediments are authigenic, and their
86 composition represents a derivative carrying the geochemical signature of average climatology.
87 We obtained modern-day monthly climatology with a particular interest in Sea Surface Salinity
88 (SSS) (Reagan et al., 2024) and moisture flux (Trenberth and Fasullo, 2022), which are
89 important estimates described in the present reconstruction. The observation shows high SSS
90 coupled with positive moisture flux coinciding with the period of SASM (June to September)
91 (Fig. 1b). This is aligned with independent observation on the increased freshwater discharge
92 of the Ganges-Brahmaputra river basin feeding BoB (Fig.1c) (Jana et al., 2015). This implies
93 the importance of CWBoB as a moisture source for continental rainfall in the modern-day
94 context, largely similar in paleo-perspective due to minimal change in continental
95 configuration during the Glacial-Interglacial period. This interpretation is substantiated by a
96 moisture transport study based on a stable oxygen isotope in rainfall collected over BoB and
97 South Asia during the period of SASM (Dar and Ghosh, 2016). The influence of riverine
98 freshwater reaching the location of the present study is found to have minimal events in the
99 regional ocean general circulation model experimental with and without riverine input (Behara



100 and Vinayachandran, 2016), making the site a test bed for reconstruction of rainfall over the
 101 oceanic setting.



102

103 **Figure 1: Site map and climatology.** a) modern-day climatology (1998 – 2019) showing the
 104 distribution of rainfall minus evaporation (mm/day) and wind vectors during the period of
 105 SASM monsoon (June, July, August and September) (Kalnay et al., 1996; Schneider et al.,
 106 2013). The study site, MGS17/GC02 (depicted as a filled orange diamond with a black
 107 boundary), along with other locations (represented by light yellow-filled circles with black
 108 boundaries), are utilized in the discussion; b) Plot of monthly Sea Surface Salinity (Reagan et
 109 al., 2024) and moisture flux (Trenberth and Fasullo, 2022) distribution over the study site
 110 (MGS17/GC02) obtained from world ocean atlas climatology resolved at 4°x4° grid space c)
 111 Long-term average monthly river discharge of Ganges and Brahmaputra to BoB (Jana et al.,
 112 2015).

113

114 The age-depth model was established utilizing 7 (¹⁴C) radiocarbon dates obtained from two
 115 species of planktic Foraminifera (*G.ruber* and *G.sacculifer*), revealing sedimentation ages



116 ranging from 3.6 (at 0.41 m core depth) to 32.9 (at 4.30 m core depth) kiloyears before present
117 (kyr BP) (Fig. S1 & Table S1). Bayesian statistics (Bacon) is used to estimate the median age
118 with uncertainty for the sedimentary layer (Fig. S1) (Blaauw and Christen, 2011).

119 Here, we conducted carbonate clumped isotope thermometry and stable isotope ($\delta^{18}\text{O}$ & $\delta^{13}\text{C}$)
120 investigation on planktic foraminifer *G. ruber* across the 18 (+1 replicate) sedimentary depth
121 with an average time window between each depth of 1.7 kyr, covering the time interval 0-31
122 kyr BP. The planktic foraminifera *G. ruber*, a surface-dwelling species, thrives at water depths
123 of 17 ± 20 meters (Lakhani et al., 2022) and is present throughout the year (Maeda et al., 2022;
124 Guptha et al., 1997), rendering it suitable for reconstruction of surface ocean hydrography
125 using the geochemical signatures in its carbonate shell. A strong correlation is observed in $\delta^{18}\text{O}$
126 record of *G. ruber* from surface sediment (top 0-1 cm) with estimated $\delta^{18}\text{O}$ values of *G. ruber*
127 using collated observation on seawater $\delta^{18}\text{O}$ values (Table S2) and satellite-based
128 climatological mean SST values (1991-2020) over BoB during the period of SASM (Fig. S2).
129 The sedimentary pack of top 1cm represents less than 100 years of accumulated sediments
130 deduced from the average sedimentation rate (Table S1). We used species-specific oxygen
131 isotope thermometry to generate the spatial pattern of $\delta^{18}\text{O}$ in *G. ruber* carbonate (Mulitza et
132 al., 2003).

133 The carbonate clumped isotopes provide a means to reconstruct the equilibrium temperature of
134 carbonate precipitation independent of the isotopic composition of ambient water (Ghosh et
135 al., 2006; Tripathi et al., 2010; Zaarur et al., 2013; Peral et al., 2018; Daëron and Gray, 2023;
136 Meinicke et al., 2020). The clumped isotope of *G. ruber*-based SST and $\delta^{18}\text{O}$ record in *G. ruber*
137 provide means to reconstruct the equilibrium surface seawater $\delta^{18}\text{O}_{\text{sw}}$ (details in methods). The
138 regional hydrological cycle was reconstructed using estimated $\delta^{18}\text{O}_{\text{sw}}$.



139 For the first time, we propose a proxy for reconstructing qualitative cloud cover intensity using
140 the planktic foraminiferal abundance ratio of *Globigerina bulloides* to *Neogloboquadrina*
141 *dutertrei*, which thrives in different water depths with significant variability in Chlorophyll a
142 concentration, making it sensitive to the presence of clouds. To quantify cumulative temporal
143 variations in continental runoff and rainfall over the NBoB, we estimated changes in SSS
144 (Δ SSS) at two different sites with varying distances from the coast. We treated the present site
145 as open marine with minimal continental runoff compared to the site in proximity to the GBM
146 river mouth (126-KL) (Fig.1a). Clumped isotope thermometry was used for SST reconstruction
147 at the present site, while SST at site KL-126 was based on the alkenone unsaturation index
148 (Kudrass et al., 2001). The temporally distinct SSS for each site was estimated from $\delta^{18}\text{O}_{\text{sw}}$,
149 assuming a steady-state Rayleigh oxygen isotope fractionation model with freshwater (rainfall
150 & continental runoff) and evaporation as input and output fluxes to the BoB surface water
151 reservoir (details in the methods section).

152 **2. Materials and Methods:**

153 **2.1 Site location and processing of sediment samples:**

154 The present sampling effort was part of an Exclusive Economic Zone expedition conducted by
155 the National Centre for Polar and Ocean Research, Ministry of Earth Sciences, India, aboard
156 RV MGS Sagar (MGS-17) during June-July 2017. The gravity core was retrieved from CW
157 BoB (15°19'36" N, 84°54'03" E) at the water depth of 2986m (Fig. 1). Our sampling effort
158 yielded a 4.3m sediment core, which was sub-sampled onboard at 1cm resolution for our
159 investigation. Each sample was processed onboard, including drying at 50°C in a hot-air oven
160 for moisture removal and storage in ziplock containers. The samples were transported to the
161 lab and further processed to remove organics using H_2O_2 and sieved to obtain appropriate size
162 fractions. These fractions were subsequently used for age determination and clumped and
163 stable isotope analysis.



164 **2.2 Age - Depth model:**

165 The age-depth model is proposed based on analysis of mixed species of planktic Foraminifera
166 (*Globigerinoides ruber* & *Globigerinoides sacculifer*) separated from samples placed at 7
167 depth intervals (Fig. S1& Table S1). The radiocarbon age determination is conducted at the
168 Physical Research Laboratory, India, using a 1MV Accelerator Mass Spectrometer. The ¹⁴C-
169 AMS dates were corrected for the reservoir age offset based on available observations from the
170 Bay of Bengal (Dutta et al., 2001). This was further adjusted to the calibrated age (before the
171 present of 1950AD; BP) using calibration software Calib 8.20 (Reimer et al., 2013; Stuiver and
172 Reimer, 1993). The calibrated dates range from 3580 year BP (41 cm depth) to 32880 year BP
173 (430 cm depth). In order to establish the sedimentation rate, we assumed the first 1cm core-top
174 sample as a representation of modern-day (1950 AD). Detailed methodology for sample
175 analysis and standard reproducibility is provided in the published literature (Bhushan et al.,
176 2019b, a). We assigned age with uncertainty to each stratum using the Bayesian statistical
177 (Bacon) method (Fig. S1) (Blaauw and Christen, 2011). Our observation showed variability of
178 sedimentation rate from 3.86 cm/kyr to 40.35 cm/kyr. A higher sedimentation rate was observed
179 during the last glacial and late hemispheres, while it was attained at a minimum during
180 deglaciation and early hemispheres (Table S1). A strong coherence of $\delta^{18}\text{O}$ variability in *G.*
181 *ruber* was observed in multiple sites adjacent to our core location (Rashid et al., 2011; Govil
182 and Divakar Naidu, 2011; Clemens et al., 2021) confirming the proposed age-depth model
183 (Fig.S3).

184 **2.3 Stable and clumped isotope analysis in *G.ruber*:**

185 The present study is based on sediment column samples ranging in age from 0 to 31 kyr BP
186 with a total of 19 samples (18 samples + 1 replicate). The planktic Foraminifera used here is
187 *Globigerinoides ruber*, which is most abundant and ubiquitous in the entire succession. The



188 sediment size fraction of 250–355 μm yielded 8-10 mg of *G. ruber* specimens required for our
189 analysis. These specimens were initially crushed and treated with 1% H_2O_2 and Sodium
190 Hydroxide buffer to remove any organic matter, further ultrasonicated with methanol to
191 dislodge clays bound within the foraminiferal skeleton, and finally removed by flotation (Peral
192 et al., 2018). These samples were dried at 50°C inside a hot air oven to remove moisture prior
193 to analysis.

194 The break-seal method is followed for the preparation of CO_2 by reacting carbonate powder 8-
195 10mg with 105% H_3PO_4 in an isolated chamber at a constant temperature of 25°C for 18 hours
196 inside a water bath. The product CO_2 is cryogenically extracted and purified for any
197 contamination using a porapak-Q GC column held at 25°C (Fosu et al., 2018). The clean CO_2
198 is transferred in an ampule and introduced in a dual inlet peripheral coupled with MAT 253
199 IRMS configured with a 44-49 mass Faraday cup. The analysis is performed at a major ion
200 beam intensity of 10V. The working reference gas for dual inlet measurement was sourced from
201 Linde AG, Munich, Germany, with specifications of 99.999% CO_2 . It was assigned a value of
202 $\delta^{13}\text{C}$ of -3.92 ± 0.01 ‰ VPDB and a $\delta^{18}\text{O}$ of 25.58 ± 0.01 ‰ VSMOW, based on repeat analysis
203 of NBS19 CO_2 from carbonate reactions.

204 Each analytical task consists of a sequence of 5-10 acquisitions, with each acquisition
205 comprising 10 cycles of sample and working reference CO_2 measured alternately. Sample and
206 working reference CO_2 are recovered back following analysis into quartz tube and heated at
207 1000°C in a muffle furnace for 3 hours to achieve stochastic distribution and defined standard
208 reference CO_2 (heated gas). These heated gases were further processed using the cryogenic
209 extraction protocol, followed by cleaning using the Porapak-Q column purged with helium.

210 Multiple heated gases of different bulk compositions are analyzed to correct for non-linearity
211 and conversion to the heated gas scale (Huntington et al., 2009). Subsequently, these



212 measurements were transformed into an Absolute Reference Frame (ARF) through a
213 combination of carbonate reference materials with assigned Δ_{47} values, including MARJ1,
214 OMC, ETH1, and ETH3.

215 The $\delta^{13}\text{C}$ and $\delta^{18}\text{O}$ values of the sample carbonate are assigned with respect to VPDB, analysing
216 interlaboratory reference MARJ1 calcite. The $\delta^{13}\text{C}$ and $\delta^{18}\text{O}$ values of MARJ1 are +1.97‰
217 and -2.02‰, respectively, established performing experiment with NBS19 as the primary
218 standard (Ghosh et al., 2005). Routine analysis of MARJ1 carbonate is carried out during the
219 sample analysis to monitor the long-term variability and performance of the setup. The long-
220 term reproducibility of $\delta^{13}\text{C}$ and $\delta^{18}\text{O}$ values of MARJ1 is 0.01‰ and 0.02‰, respectively.

221 **2.4 Temperature Estimates Based on Clumped Isotope (Δ_{47}) with Uncertainty:**

222 The most updated calibration (Zaarur et al., 2013) proposed at 25°C acid-carbonate digestion
223 of inorganic and biogenic (Foraminifera) carbonate precipitation at a known temperature range
224 of 5°C to 65°C is used for estimation of temperature. The analytical protocol used for this
225 calibration closely matches the present study. The broad temperature range explored in this
226 calibration exercise facilitated the appropriate reconstruction of surface ocean temperatures
227 during the Glacial-Interglacial time. The error propagation due to analytical and calibration
228 uncertainties is estimated using the suggested algorithm (Huntington et al., 2009).

229 **2.5 Estimation of $\delta^{18}\text{O}_{\text{sw}}$ and error propagation:**

230 The simultaneous measurement of temperature using carbonate clumped (Δ_{47}) isotopes
231 together with stable oxygen isotopic composition ($\delta^{18}\text{O}$) measured in *G.ruber* allows the
232 reconstruction of $\delta^{18}\text{O}_{\text{sw}}$ in seawater. We employed the relationship between the $\delta^{18}\text{O}$
233 fractionation between inorganic calcite and water and carbonate precipitation temperature



234 (Kim and O’Neil, 1997) to estimate the equilibrium $\delta^{18}\text{O}_{\text{sw}}$ for our sample. This relationship
235 has been verified for foraminiferal carbonates (Peral et al., 2018; Daëron and Gray, 2023).

236 The extent of ice volume locked in continental ice sheets also regulates $\delta^{18}\text{O}_{\text{sw}}$ and is taken into
237 account for appropriate estimation of $\delta^{18}\text{O}_{\text{sw}}$. This was accomplished using the equation
238 (Adkins et al., 2002):

$$239 \quad \delta^{18}\text{O}_{\text{sw-ivc}} = \delta^{18}\text{O}_{\text{sw}} + (\text{SL} * 0.0083)$$

240 Where $\delta^{18}\text{O}_{\text{sw-ivc}}$ is ice volume corrected $\delta^{18}\text{O}_{\text{sw}}$, and SL is coral-based sea-level estimates
241 (Lambeck et al., 2014). The error associated with $\delta^{18}\text{O}_{\text{sw-ivc}}$ are estimated by propagating the
242 errors in SST, and $\delta^{18}\text{O}_{G.ruber}$ measurements are given as:

$$243 \quad \sigma_{\delta^{18}\text{O}_{\text{sw-ivc}}}^2 = \left(\frac{18030}{\text{SST}^2} \sigma_{\text{SST}} \right)^2 + (\sigma_{\delta^{18}\text{O}_{G.ruber}})^2$$

244 **2.6 Quantifying the change in SSS between NBoB and CWBoB (ΔSSS):**

245 The conventional approach to estimating SSS in the Glacial-Interglacial context typically
246 involves assuming that the modern-day slope and intercept are derived from the correlation
247 between $\delta^{18}\text{O}_{\text{sw}}$ and SSS (Govil and Divakar Naidu, 2011). The slope and intercept of this linear
248 regression equation vary due to differential freshwater fluxes, including runoff and oceanic
249 rainfall (Singh et al., 2014). This variable behavior of freshwater fluxes contributes to the
250 overall uncertainty in SSS estimation in the palaeo-reference frame (Mehta et al., 2021). In
251 order to avoid such complications in SSS estimation, here we used a steady-state Rayleigh
252 oxygen isotope fractionation model. This model integrates freshwater flux (rainfall and river
253 runoff) and evaporation as input and output fluxes to the surface ocean reservoir of the Bay of
254 Bengal (for detailed mathematical derivation, refer to (Singh et al., 2014)). The TraCE-21k
255 climate model simulation outputs of rainfall and evaporation over the Indian Subcontinent and
256 the Bay of Bengal are used as flux values in the Rayleigh model (Table S4). The TraCE-21k



257 climate model simulation reproduced the proxy-based estimates with reasonable satisfaction
258 (Jalihal et al., 2019, 2020). Assuming an initial composition of the surface ocean reservoir as
259 0‰ without any freshwater flux, the relationship between SSS and $\delta^{18}\text{O}_{\text{sw}}$ is expressed as
260 follows:

$$261 \quad \frac{\text{SSS}}{S_0} = \left[\frac{\delta^{18}\text{O}_{\text{sw}} \times (1 - \beta)}{(\beta \times \delta^{18}\text{O}_{\text{freshwater}}) - \varepsilon_{\text{vap/liq}}} \right] + 1$$

262

263 Where $S_0 = 34.8$ psu represents the mean salinity state of the deep ocean, defined as the initial
264 salinity reference state. β denotes the ratio of fluxes of freshwater to the evaporation. We
265 assumed Last Glacial Maximum (LGM) fluxes for the period post-LGM which lies between
266 the time interval of 21-31 kyr BP. The average isotopic composition of freshwater ($\delta^{18}\text{O}_{\text{freshwater}}$)
267 is -6.1‰, estimated here by considering different fluxes and their isotopic values from the
268 literature and weighing them with proportionate contribution (Table S3). The oxygen isotopic
269 fractionation between vapor and liquid phases during evaporation is represented as $\varepsilon_{\text{vap/liq}}$.
270 Under equilibrium conditions, the SST governs the isotopic composition of vapor (Horita and
271 Wesolowski, 1994). However, the actual vapor tends to be 2-5‰ heavier than expected at
272 equilibrium due to the involvement of kinetic processes (Merlivat and Jouzel, 1979). Therefore,
273 we adopted $\varepsilon_{\text{vap/liq}}$ to be 5‰ heavier than the equilibrium state. Applying this method, we
274 estimated the SSS at the study sites in the CWBoB (MGS17/GC02) and NBoB (KL-126), and
275 reported the change in SSS (ΔSSS) between these two regions (Table S5). The $\delta^{18}\text{O}_{\text{sw}}$ for the
276 KL-126 site was estimated using the same procedure discussed in Section 2.5, employing
277 alkenone unsaturation index-based SST and the $\delta^{18}\text{O}$ of *G. ruber* (Kudrass et al., 2001). The
278 error propagation associated with ΔSSS estimation is provided in the supplementary text.

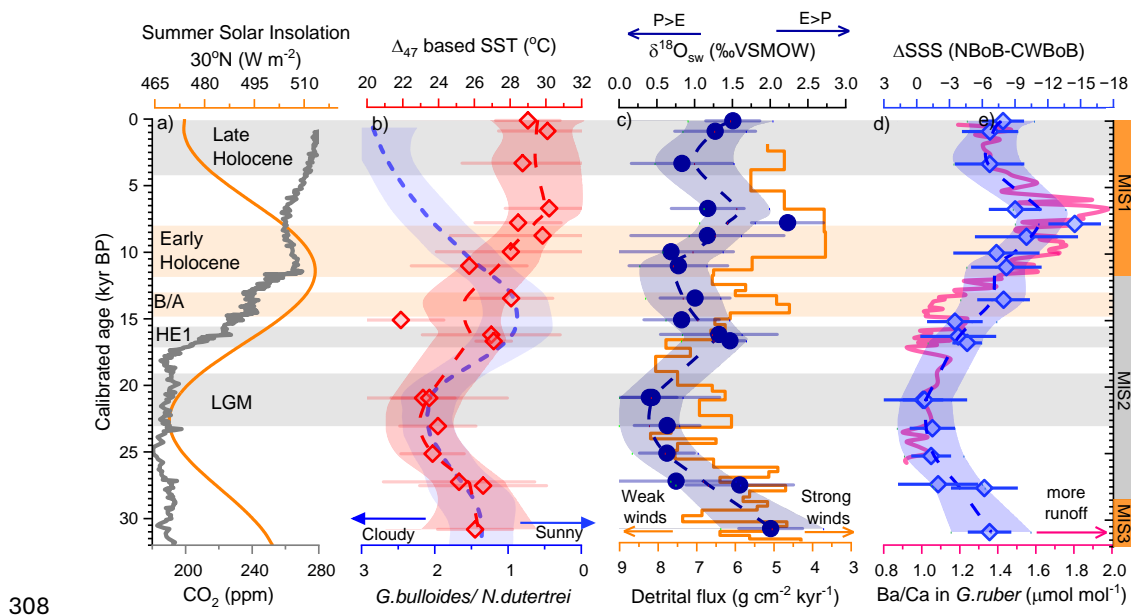


279 **3. Results and Discussion:**

280 Below, we describe the stable ($\delta^{18}\text{O}$) and clumped isotopic composition in planktic
281 foraminiferal carbonates (*G.ruber*) at 18 (+1 replicate)- different time intervals across the
282 sedimentary section encompassing a time interval from 0 to 31 kyr BP located at the Central-
283 West BoB (MGS17/GC02). The $\delta^{18}\text{O}$ values of *G. ruber* varied between -2.0‰ and +0.4‰,
284 with the heaviest values recorded during the Last Glacial period and the early stages of
285 deglaciation (15.1-30.9 kyr BP; average $\delta^{18}\text{O}$ value of $-0.1 \pm 0.2\text{‰}$; n=11) (Table S4).
286 Progressively, with younging in the sedimentary strata, the $\delta^{18}\text{O}$ value decreased from +0.2‰
287 to -1.8‰ denoted by the time interval of late deglaciation (15.1 kyr BP) to the Early Holocene
288 (9.9 kyr BP) (Table S4). The Holocene (0 to 10.9 kyr BP) is characterized by a lighter average
289 $\delta^{18}\text{O}$ value of $-1.6 \pm 0.5\text{‰}$ (n=8) (Table S4). The robust consistency in $\delta^{18}\text{O}$ variability in *G.*
290 *ruber* in the present study and the data from the adjacent sites (VM29-19(Rashid et al., 2011),
291 SK218/1(Govil and Divakar Naidu, 2011), and IODP 353 site U1446 (Clemens et al., 2021))
292 suggest similarity of sea surface temperature and salinity variation in the spatial domain (Fig.
293 S3). While the $\delta^{18}\text{O}$ value of planktic foraminiferal carbonate represents habitat temperature
294 and the composition of seawater $\delta^{18}\text{O}$, clumped isotope thermometry provides a unique method
295 to ascertain temperature for carbonate precipitation in equilibrium without reliance on the
296 ambient water's $\delta^{18}\text{O}$ composition (Ghosh et al., 2006; Zaarur et al., 2013; Daëron and Gray,
297 2023; Meinicke et al., 2020; Peral et al., 2018; Tripathi et al., 2010). The clumped isotope (Δ_{47})
298 values range from 0.681 to 0.716‰ (Table S4), with heavier values observed during MIS 3 and
299 the early part of MIS 2, including the LGM, with an average value of $0.704 \pm 0.006\text{‰}$ (n=7)
300 representing the time interval from 20.9 to 30.9 kyr BP. The Δ_{47} value decreased from 0.716‰
301 to 0.683‰ during the later part of deglaciation and Early Holocene (8.7-15.1 kyr BP). The
302 lowest average Δ_{47} value of 0.684 ± 0.003 (n=6) was observed during the latest part of the
303 Holocene (0-8.7 kyr BP). The clumped isotope values are converted into temperature using the



304 relevant empirical correlation tailored for the foraminiferal carbonates (Zaarur et al., 2013).
 305 Upon estimating the paleo-SST at different time intervals, $\delta^{18}\text{O}$ records of carbonates are used
 306 for deriving $\delta^{18}\text{O}$ of seawater ($\delta^{18}\text{O}_{\text{sw}}$), which was corrected for the ice-volume effect (detail
 307 provided in methods).



308
 309 **Fig. 2: Proxy-based records of hydroclimate, Sea Surface Temperature, and its physical**
 310 **drivers over the Bay of Bengal and South Asia for the past 31 kiloyears.** a) Summer (June)
 311 time solar insolation at 30°N (Berger, 1992) and global atmospheric CO₂ concentration record
 312 from Antarctica ice core (Bereiter et al., 2015). b) Clumped isotope (Δ_{47} of carbonate) of
 313 *G. ruber* derived SST from site MGS17/GC02 and cloud cover proxy of *G. bulloides/N. dutertrei*
 314 from site SK218. c) $\delta^{18}\text{O}_{\text{sw}}$ from the site MGS17/GC02 (CWBoB) compared with SASM wind
 315 proxy of eolian detrital flux (Pourmand et al., 2004). d) Estimated ΔSSS between NBoB and
 316 CW BoB suggest cumulative freshwater flux to NBoB and Ba/Ca ratio in *G. ruber* record from
 317 NBoB suggesting continental runoff (Weldeab et al., 2022).



318 **3.1 Temporal dynamics of SST during the past 31 kilo years:**

319 The SST reconstructed from carbonate clumped isotope (Δ_{47}) data of *G. ruber* over the time
320 interval of past 31 kyr ranges between 22°C to 30°C (Fig. 2b). Chronologically, the MIS3 and
321 early phases MIS2, which encompasses a time interval between 27.8-30.9 kyr BP is
322 characterized by warm average SST (± 1 SD) of $26 \pm 0.7^\circ\text{C}$ ($n=3$) (Fig. 2b). This is overlain by
323 sediments denoting mid-phase of MIS2 and LGM (20.9-25.2 kyr BP) recording lowest average
324 SST (± 1 SD) of $24 \pm 0.3^\circ\text{C}$ ($n=4$). The deglaciation time interval (13.4 - 20.9 kyr BP) recorded
325 a monotonic increment in the SST values by 5°C (Fig. 2b). The younger sedimentary sequence
326 above this represents a time interval of Early Holocene (8.7 - 10.9 kyr BP) which is marked
327 with average warmer SST (± 1 SD) of $28 \pm 2^\circ\text{C}$ ($n = 3$) (Fig. 2b). The mid and late Holocene (0
328 – 7.7 kyr BP) characterized by stable warm SST (± 1 SD) of $29 \pm 0.8^\circ\text{C}$ ($n = 5$) (Fig. 2b).

329 The average SST difference between the Late Holocene and the LGM in the present study is
330 5°C, contrasting with the 3°C difference recorded by Mg/Ca ratio-based SST reconstruction in
331 *G. ruber* from the region of BoB (Clemens et al., 2021; Rashid et al., 2011; Raza et al., 2017;
332 Govil and Divakar Naidu, 2011). The discrepancy in SST difference can be explained by the
333 involvement of non-thermal variables, which include salinity and pH, influencing the Mg/Ca
334 ratio in *G. ruber*, causing an underestimation of temperature using this approach (Gray and
335 Evans, 2019). The organic geochemical proxies-based SST reconstruction, such as the
336 alkenone unsaturation index ($U^{k'}_{37}$) (Kudrass et al., 2001; Sonzogni et al., 1998), and TEX_{86}
337 (TetraEther index of tetraethers consisting of 86 carbon atoms) (Clemens et al., 2021), recorded
338 a 2°C difference. These proxies are unaffected by seawater chemistry. However, $U^{k'}_{37}$ faces a
339 significant limitation in that it becomes insensitive to temperatures above 29°C (Müller et al.,
340 1998). Additionally, TEX_{86} may primarily reflect subsurface conditions in certain
341 oceanographic settings (Rommerskirchen et al., 2011). Moreover, both $U^{k'}_{37}$ and TEX_{86} exhibit



342 seasonal bias when representing SST (Chen et al., 2014; Sonzogni et al., 1998; Wuchter et al.,
343 2006).

344 The application of the empirical relationship between the abundance of planktic foraminiferal
345 species with temperature recorded SST shift of 0-2°C over the region of BoB (Cullen, 1981).

346 The $\delta^{18}\text{O}$ record in *G.ruber*-based SST shift with an assumption of constant $\delta^{18}\text{O}$ composition
347 of seawater registered 1°C cooling during LGM compared to Late Holocene (Duplessy, 1982).

348 The clumped isotope (Δ_{47}) based SST reconstruction in *G. ruber* is independent of non-thermal
349 variables like pH and salinity beside the isotopic composition of environmental seawater,
350 making this a superior technique for temperature reconstruction (Tripathi et al., 2010; Peral et
351 al., 2018).

352 We matched the present SST record over the time interval of the past 31 kyr with global ice
353 core CO_2 concentration and summer (June) solar insolation at 30°N to understand the role of
354 internal and external earth system forcing. Our observation explains 54% and 8% variability of
355 SST with changes in the CO_2 concentration and solar insolation, respectively (Fig.S4),
356 confirming the climate sensitivity analysis from climate model output (Araya-Melo et al.,
357 2015).

358 The variation in the SST values during the past 31 kyr is explained by combining summer solar
359 insolation and atmospheric CO_2 forcing together, modulating the process of upwelling and
360 cloud cover associated with convective rainfall. The upwelling process promotes the transfer
361 of cold subsurface water, while cloud cover associated with convective rainfall determines the
362 extent of solar radiation reaching the surface water. The upwelling process can be understood
363 through paleo-productivity proxies, such as biogenic silica records from the BoB, which
364 indicate weak upwelling from the Last Glacial to the Early Holocene and strong upwelling
365 during the Mid-Holocene (Liu et al., 2021).



366 **3.2 Effect of cloud cover on SST:**

367 The cloud cover plays a pivotal role in regulating Photosynthetically Active Radiation (PAR)
368 over the ocean, thereby influencing the depth of maximum Chlorophyll a (Chl a) through
369 mechanisms such as photoacclimation and chlorophyll re-organization (Jyothibabu et al., 2018;
370 Masuda et al., 2021). Elevated light intensity induces the contraction and aggregation of
371 chloroplasts within phytoplankton cells, reducing their efficiency in absorbing light and Chl a
372 content (Kiefer, 1973). Consequently, this triggers the vertical migration of Chl a, leading to
373 its accumulation in regions characterized by low PAR (Jyothibabu et al., 2018).

374 Studies conducted during the SASM monsoon period have demonstrated a notable shift in the
375 water depth of Chl a maxima between cloudy and sunny days, ranging from surface levels to
376 40 meters and 40-80 meters water depth over the BoB, respectively (Jyothibabu et al., 2018);
377 identified using onboard observation in the region of BoB. The abundance of planktic
378 foraminifera is sensitive to Chl a concentrations (Munir et al., 2022; Kuroyanagi and Kawahata,
379 2004). Specifically, two species, *Globigerina bulloides*, and *Neogloboquadrina dutertrei*,
380 exhibit maximal thriving conditions at water depths of 0-50 meters and 50-100 meters,
381 respectively (Tapia et al., 2022) (Fig.S5).

382 Drawing upon the relationship between cloud cover and the depth of Chl a maxima, as well as
383 the influence of Chl a on planktic foraminiferal abundance, we propose a proxy for cloud cover
384 utilizing the ratio of planktic foraminiferal abundance of *G. bulloides* to *N. dutertrei*. A
385 significant negative correlation is evident between reanalysis data of outgoing longwave
386 radiation, serving as an index for cloud cover, and the ratio of *G. bulloides* to *N. dutertrei*, as
387 revealed by sediment trap records from the NBoB (Pearson's r value = -0.61 , p -value = 0.03,
388 n = 13) and CBoB (Pearson's r value = -0.74 , p -value = 0.004, n = 13) (Guptha et al., 1997)
389 (Fig. S6). The relatively weak relationship and differential slope observed over NBoB
390 compared to CBoB may be attributed to the influence of riverine suspended sediments, which



391 also modulate the relationship between PAR and the depth of Chl a maxima (Jyothibabu et al.,
392 2018). This framework enables the reconstruction of paleo-cloud cover using temporal
393 variation in the ratio of *G. bulloides* to *N. dutertrei*. It is important to mention that the upwelling
394 process also contributes to the shifting of the depth of Chl a maxima (Garg et al., 2024), thereby
395 contributing to the populational abundance of *G. bulloides* (Prell and Curry, 1981). The SASM
396 monsoon also generates upwelling along the eastern margin of India (Shetye et al., 1991).
397 However, the observation showed weaker upwelling at the site of the present study with
398 confinement near the coast because of the strong stratification (Shetye et al., 1991;
399 Gopalakrishna and Sastry, 1985).

400 We adapted the planktic foraminiferal abundance data recorded in the sediment core of the
401 adjacent site SK218 (Verma et al., 2022) to derive information about the role of cloud cover on
402 regional SST. Given the weak upwelling activity between Early Holocene and Last Glacial
403 based on biogenic silica mass accumulation rate (Liu et al., 2021), cloud cover emerged as the
404 primary factor modulating the ratio of *G. bulloides* to *N. dutertrei*. The high and low ratio
405 values of *G. bulloides* to *N. dutertrei* during the LGM and the deglaciation to Early Holocene
406 periods indicate periods of high and low cloud cover, respectively. However, during the middle
407 Holocene, the high ratio of *G. bulloides* to *N. dutertrei*, coupled with high biogenic silica
408 content (Liu et al., 2021), suggests that both cloud cover and upwelling were dominant factors.
409 The temporal correlation observed between the ratio of *G. bulloides* to *N. dutertrei* and changes
410 in SST (Fig. 2b), as inferred from our Δ_{47} -based temperature reconstructions, suggests that
411 cloud cover has significantly influenced SST dynamics during the time interval of 16-31 kyr
412 BP in the CW BoB. From 16 kyr BP to 0 kyr BP, SST in the CWBoB increased despite a rise
413 in cloud cover (Fig. 2b). This warming trend can be attributed to radiative forcing associated
414 with elevated atmospheric CO₂ levels (Fig. 2a & 2b).



415 **3.3 Evaporation versus Rainfall over CW BoB regulated by wind:**

416 SASM is characterised by SW trade wind, which promotes evaporation and release of latent
417 heat over the region of CW BoB (Samanta et al., 2018) and transports moisture to the region
418 of NBoB and South Asia (Dar and Ghosh, 2016; Yoon and Chen, 2005). Here, we took
419 advantage of the estimated $\delta^{18}\text{O}_{\text{sw}}$ at CW BoB to reconstruct the moisture imbalance due to the
420 process of evaporation and rainfall (Fig. 2c). The strength of SASM wind during this time
421 interval is derived from eolian detrital flux from the northeastern Arabian Sea (Pourmand et
422 al., 2004) (Fig. 2c). The eolian input to this region is transported from the Arabian Peninsula
423 and Persian Gulf during periods of weak SASM winds and strong northwesterly. Conversely,
424 the eolian input is minimal during periods of strong SASM winds (Pourmand et al., 2004).

425 The $\delta^{18}\text{O}_{\text{sw}}$ record from CWBoB exhibits a robust temporal correlation with the SASM wind
426 speed proxy (eolian detrital flux) spanning the past 31 kyr (Fig. 2c). Lighter $\delta^{18}\text{O}_{\text{sw}}$ values
427 observed during the early phase of MIS 2 (20.9 – 27.6 kyr BP; including LGM), the
428 deglaciation to Early Holocene transition (9.9 – 13.4 kyr BP), and the mid to late Holocene
429 transition (3.2 – 6.6 kyr BP) indicate surplus rainfall relative to evaporation over the CW BoB
430 (Fig. 2c). This phenomenon is linked to weakened SASM wind speeds, reducing the quantum
431 of moisture transported to the NBoB and South Asia, thereby exacerbating aridity on the
432 continent (Fig. 2c) (Kudrass et al., 2001; Dutt et al., 2015).

433 Conversely, heavier $\delta^{18}\text{O}_{\text{sw}}$ compositions during the MIS 3 to MIS 2 transition (27.6 – 30.9 kyr
434 BP), Heinrich Event 1, and the Early to mid-Holocene transition (6.6 – 9.9 kyr BP) suggest an
435 excess of evaporation compared to rainfall over the CW BoB (Fig. 2c). This trend is associated
436 with intensified SASM winds (Fig. 2c) and increased continental rainfall and river runoff,
437 indicating moisture transport from CWBoB to South Asia (Kudrass et al., 2001; Dutt et al.,
438 2015; Weldeab et al., 2022). In summary, the fluctuation in evaporation over rainfall in the CW



439 BoB over the past 31 kyr implies a meridional shift in the intensity of convective rainfall clouds
440 during this period.

441 **3.4 Moisture transport to the continent in response to SST over CW BoB:**

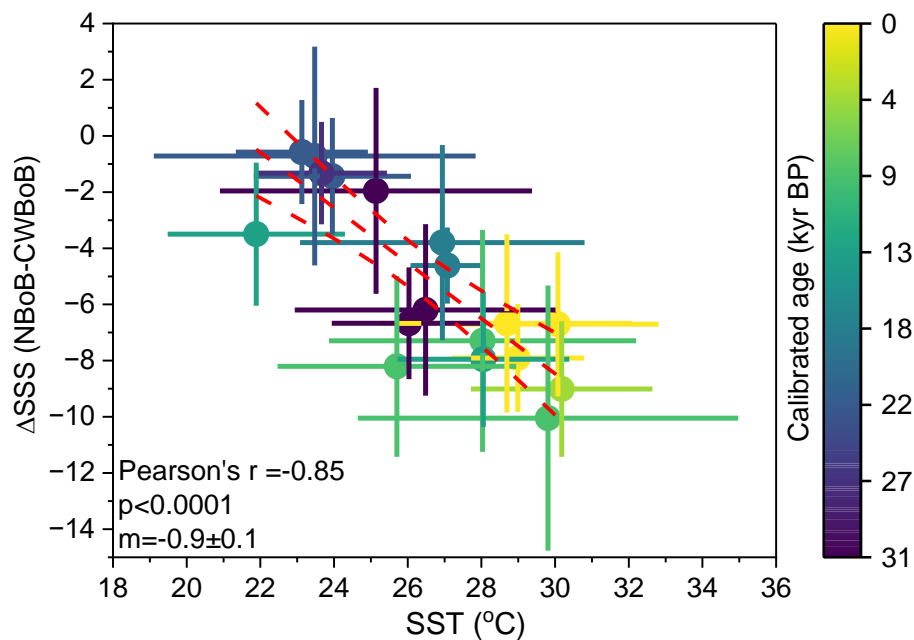
442 The moisture transport to South Asia and NBoB is driven by two primary physical factors,
443 which include evaporated moisture flux from CW BoB together with wind, which propel the
444 water vapor parcel to reach the coastal region and continental landmass (Dar and Ghosh, 2016;
445 Yoon and Chen, 2005; Shenoi, 2002; Samanta et al., 2018). The contribution of moisture flux
446 varies with changes in SST, while the transport is governed by the pressure difference between
447 ocean and continental landmass (Samanta et al., 2018; Goswami, 1987). The region of CW
448 BoB during SASM time based on modern-day observation shows the intensification of the
449 evaporation process with higher SST (Samanta et al., 2018). The sensitivity of this process
450 varied during Glacial and Inter-glacial time frames with 8°C change in the SST condition over
451 CWBoB (Fig. 2b). The proportion of this moisture distribution into the NBoB as rainfall and
452 continental runoff can be understood with an independent record of reconstructed $\delta^{18}\text{O}_{\text{sw}}$
453 variability across Glacial and Interglacial time interval. To quantify the cumulative freshwater
454 influx into the NBoB, we estimated the difference in $\delta^{18}\text{O}_{\text{sw}}$ ($\Delta^{18}\text{O}_{\text{sw}}$) between the coastal site
455 KL-126 in the NBoB (Kudrass et al., 2001) and the present study site MGS17/GC02 in the CW
456 BoB. The $\delta^{18}\text{O}_{\text{sw}}$ over BoB is related to Sea Surface Salinity (SSS), which is modeled using an
457 oxygen isotope-based Rayleigh steady-state model with freshwater and evaporation as input
458 and output to the surface seawater reservoir (Singh et al., 2014). The ($\Delta^{18}\text{O}_{\text{sw}}$) is used for the
459 estimation of changes in SSS (ΔSSS) between NBoB and CW BoB for the Glacial-Interglacial
460 time interval, which translates into a relative change in rainfall over South Asia and continental
461 runoff to NBoB (Fig. 2d & Table S4). The temporal pattern of ΔSSS is in accordance with
462 Ba/Ca ratio of *G.ruber*-based continental runoff proxy from the region of NBoB, which reflects
463 SASM rainfall intensity over the continental region (Weldeab et al., 2022) (Fig. 2d).



464 The higher average ($\pm 1SD$) ΔSSS value of -1.4 ± 0.4 psu ($n = 4$) is observed during the early
465 phase of MIS 2 (20.9-28 kyr BP), prohibiting moisture transport to the continental region (Fig.
466 2d & Table S4). This is consistent with our observation of the high ratio of *G. bulloides* to *N.*
467 *dutertrei* abundances, denoting the presence of convective cloud cover over the region of CW
468 BoB (Fig. 2b).

469 The lower average ($\pm 1SD$) ΔSSS value of -11.2 ± 2.9 psu ($n = 3$) is observed during the Early
470 to Mid Holocene transition (6.6 to 8.7 kyr BP), corresponding to a period of excess continental
471 runoff over NBoB (Fig. 2d). The evidence of rainfall variability in the continental region is
472 discernible in the vegetation cover, as revealed by the temporal pollen records from lake
473 sediments. These records indicate the presence of open vegetation during periods of high ΔSSS
474 and mixed tropical deciduous vegetation during periods of low ΔSSS (Quamar and Bera, 2020).

475 We observed a strong relationship between SST at CW BoB with ΔSSS denoting freshwater
476 input into the region of NBoB (Fig. 3). This relationship is based on 18-time intervals (+1
477 replicate) in continuity in the sedimentary record, denoting average time resolution of 1.7 kyr
478 which discounts interferences from short term climatic processes such as El Niño-Southern
479 Oscillation, Indian Ocean Dipole, and North Atlantic Oscillation. The observation shows a
480 sensitivity of moisture transport as evident from a drop in ΔSSS by 0.9 ± 0.1 psu with an
481 increment of 1°C in the SST record over CW BoB (Fig. 3). Our observation identified SST as
482 a crucial factor in determining the moisture transport process and rainfall over NBoB and South
483 Asia.



484

485 **Fig. 3:** Time-integrated record showing the response of Δ SSS (NBoB-CWBoB) with SST over
486 CW BoB denotes the intensity of SASM over South Asia and NBoB during the past 31kyr BP.
487 The color grading provides measures for geological time intervals.

488

489 **4. Conclusion:**

490 This is the first record of SST variability from BoB covering the time period of the past 31 kyr
491 BP encompassing interglacial and last glacial time interval using clumped isotope thermometry
492 on *G.ruber* planktic foraminiferal carbonate. The variability in SST is predominantly driven by
493 global atmospheric CO₂ levels, accounting for 54% of the overall signal. Notably, internal
494 feedback processes involving cloud cover emerge as significant factors in SST modulation.
495 Furthermore, hydrological feedback mechanisms within the CWBoB are elucidated through



496 $\delta^{18}\text{O}_{\text{sw}}$ analysis. A strong correlation is observed between $\delta^{18}\text{O}_{\text{sw}}$ and SASM wind strength from
497 31 kyr BP to the present. The present record showed SST over CW BoB regulated the moisture
498 transport to NBoB and, in turn, contributed to freshwater discharge by rivers together with
499 rainfall. This is captured in the SSS difference between the coastal sites at NBoB and open
500 ocean site at CW BoB.

501 **Author contributions:**

502 TS and PG conceptualized the study, and PG secured project funding. TS conducted stable and
503 clumped isotope analysis on foraminifera and interpreted the data. RV, HR, AJD, and AS did
504 radiocarbon analysis. TS and PG wrote the original draft and finally reviewed and edited by all
505 authors.

506 **Competing interests:**

507 The authors declare that they have no competing interests.

508 **Acknowledgements:**

509 TS expresses gratitude to Dr. John Kurian, Dr. M. Ravichandran, the director of NCPOR, and
510 expedition chief scientist Mr. Bijesh C M for granting the opportunity to participate in the
511 scientific cruise aboard RV MGS Sagar 17 and for their assistance in collecting sedimentary
512 core samples for this study. We extend our appreciation to Dr. Partha Sarathi Jena for his
513 assistance in constructing the Bayesian age (Bacon) model. Additionally, we acknowledge Dr.
514 Arvind Singh for providing modern-day surface water oxygen isotope data over the Bay of
515 Bengal. This research benefited from project grants provided by the Department of Science &
516 Technology, India. TS acknowledges the Council of Scientific and Industrial Research,
517 Government of India, for financial support through a fellowship for PhD (File No.: 09/079
518 (2811)/2019-EMR-1), as well as the Divecha Centre for Climate Change, IISc, India, for the
519 Grantham fellowship.



520 **Data availability:**

521 All data needed to evaluate the conclusions in the paper are presented in the Supplementary

522 Table (S1-S5).

523 **Reference:**

524 Adkins, J. F., McIntyre, K., and Schrag, D. P.: The salinity, temperature, and $\delta^{18}\text{O}$ of the

525 glacial deep ocean, *Science* (80-.), 298, 1769–1773,

526 <https://doi.org/10.1126/science.1076252>, 2002.

527 Araya-Melo, P. A., Crucifix, M., and Bounceur, N.: Global sensitivity analysis of the Indian

528 monsoon during the Pleistocene, *Clim. Past*, 11, 45–61, [https://doi.org/10.5194/cp-11-45-](https://doi.org/10.5194/cp-11-45-2015)

529 2015, 2015.

530 Behara, A. and Vinayachandran, P. N.: An OGCM study of the impact of rain and river water

531 forcing on the Bay of Bengal, *J. Geophys. Res. Ocean.*, 121, 2425–2446,

532 <https://doi.org/https://doi.org/10.1002/2015JC011325>, 2016.

533 Bereiter, B., Eggleston, S., Schmitt, J., Nehrbass-Ahles, C., Stocker, T. F., Fischer, H.,

534 Kipfstuhl, S., and Chappellaz, J.: Revision of the EPICA Dome C CO_2 record from 800 to

535 600-kyr before present, *Geophys. Res. Lett.*, 42, 542–549,

536 <https://doi.org/10.1002/2014GL061957>, 2015.

537 Berger, A.: *Orbital Variations and Insolation Database.*, NOAA/NGDC Paleoclimatology

538 Program, Boulder CO, USA., 1992.

539 Berggren, W. A.: Carbon cycling in the glacial ocean: Constraints on the ocean's role in

540 global change, 80–82 pp., [https://doi.org/10.1016/0012-8252\(95\)90055-1](https://doi.org/10.1016/0012-8252(95)90055-1), 1995.

541 Bhushan, R., Yadava, M. G., Shah, M. S., Banerji, U. S., Raj, H., Shah, C., and Dabhi, A. J.:

542 First results from the PRL Accelerator Mass Spectrometer, *Curr. Sci.*, 116, 361–363, 2019a.



- 543 Bhushan, R., Yadava, M. G., Shah, M. S., and Raj, H.: Performance of a new 1MV AMS
544 facility (AURiS) at PRL, Ahmedabad, India, *Nucl. Instruments Methods Phys. Res. Sect. B*
545 *Beam Interact. with Mater. Atoms*, 439, 76–79, <https://doi.org/10.1016/j.nimb.2018.12.003>,
546 2019b.
- 547 Blaauw, M. and Christen, J. A.: Flexible paleoclimate age-depth models using an
548 autoregressive gamma process, *Bayesian Anal.*, 6, 457–474, [https://doi.org/10.1214/11-
549 ba618](https://doi.org/10.1214/11-
549 ba618), 2011.
- 550 Borah, P. J., Venugopal, V., Sukhatme, J., Muddebihal, P., and Goswami, B. N.: Indian
551 monsoon derailed by a North Atlantic wavetrain, *Science (80-.)*, 370, 1335–1338,
552 <https://doi.org/10.1126/science.aay6043>, 2020.
- 553 Chakraborty, A. and Singhai, P.: Asymmetric response of the Indian summer monsoon to
554 positive and negative phases of major tropical climate patterns, *Sci. Rep.*, 11,
555 <https://doi.org/10.1038/s41598-021-01758-6>, 2021.
- 556 Chen, W., Mohtadi, M., Schefuß, E., and Mollenhauer, G.: Organic-geochemical proxies of
557 sea surface temperature in surface sediments of the tropical eastern Indian Ocean, *Deep. Res.*
558 *Part I Oceanogr. Res. Pap.*, 88, 17–29, <https://doi.org/10.1016/j.dsr.2014.03.005>, 2014.
- 559 Clemens, S. C., Yamamoto, M., Thirumalai, K., Giosan, L., Richey, J. N., Nilsson-Kerr, K.,
560 Rosenthal, Y., Anand, P., and McGrath, S. M.: Remote and local drivers of pleistocene South
561 Asian summer monsoon precipitation: A test for future predictions, *Sci. Adv.*, 7, 1–16,
562 <https://doi.org/10.1126/sciadv.abg3848>, 2021.
- 563 Cullen, J. L.: Microfossils evidence for changing salinity patterns in the Bay of Bengal over
564 the last 20,000 years, *Palaeogeogr. Palaeoclimatol. Palaeoecol.*, 35, 315–356,
565 [https://doi.org/https://doi.org/10.1016/0031-0182\(81\)90101-2](https://doi.org/https://doi.org/10.1016/0031-0182(81)90101-2), 1981.



- 566 Daëron, M. and Gray, W. R.: Revisiting Oxygen-18 and Clumped Isotopes in Planktic and
567 Benthic Foraminifera, *Paleoceanogr. Paleoclimatology*, 38,
568 <https://doi.org/10.1029/2023PA004660>, 2023.
- 569 Dar, S. S. and Ghosh, P.: Presence of continental and Bay of Bengal moisture in rainfall at
570 Kolkata, revealed through simultaneous observation from land and sea during South-West
571 monsoon of 2004, *Earth Syst. Dyn. Discuss.*, 1–13, <https://doi.org/10.5194/esd-2016-63>,
572 2016.
- 573 Dinezio, P. N., Puy, M., Thirumalai, K., Jin, F., and Tierney, J. E.: Emergence of an
574 equatorial mode of climate variability in the Indian Ocean, *Sci. Adv.*, 6, 1–10, 2020.
- 575 DiNezio, P. N., Tierney, J. E., Otto-Bliesner, B. L., Timmermann, A., Bhattacharya, T.,
576 Rosenbloom, N., and Brady, E.: Glacial changes in tropical climate amplified by the Indian
577 Ocean, *Sci. Adv.*, 4, eaat9658, <https://doi.org/10.1126/sciadv.aat9658>, 2018.
- 578 Duplessy, J. C.: Glacial to interglacial contrasts in the northern Indian Ocean, *Nature*, 295,
579 494–498, <https://doi.org/10.1038/295494a0>, 1982.
- 580 Dutt, S., Gupta, A. K., Clemens, S. C., Cheng, H., Singh, R. K., Kathayat, G., and Lawrence
581 Edwards, R.: Abrupt changes in Indian summer monsoon strength during 33,800 to
582 5500years B.P., *Geophys. Res. Lett.*, 42, 5526–5532, <https://doi.org/10.1002/2015GL064015>,
583 2015.
- 584 Dutta, K., Bhushan, R., and Somayajulu, B. L. K.: ΔR correction values for the northern
585 Indian Ocean, *Radiocarbon*, <https://doi.org/10.1017/S0033822200038376>, 2001.
- 586 Evans, D., Bhatia, R., Stoll, H., and Müller, W.: LA-ICPMS Ba/Ca analyses of planktic
587 foraminifera from the Bay of Bengal: Implications for late Pleistocene orbital control on
588 monsoon freshwater flux, *Geochemistry, Geophys. Geosystems*,



- 589 <https://doi.org/10.1002/2015GC005822>, 2015.
- 590 Fosu, B. R., Ghosh, P., Mishra, D., Banerjee, Y., K. P., and Sarkar, A.: Acid digestion of
591 carbonates using break seal method for clumped isotope analysis, *Rapid Commun. Mass*
592 *Spectrom.*, <https://doi.org/10.1002/rcm.8304>, 2018.
- 593 Gadgil, S. and Gadgil, S.: The Indian monsoon, GDP and agriculture, *Econ. Polit. Wkly.*,
594 4887–4895, <https://doi.org/10.2307/4418949>, 2006.
- 595 Garg, S., Gauns, M., and Pratihary, A. K.: Response of oceanic subsurface chlorophyll
596 maxima to environmental drivers in the Northern Indian Ocean, *Environ. Res.*, 240, 117528,
597 <https://doi.org/10.1016/j.envres.2023.117528>, 2024.
- 598 Ghosh, P., Patecki, M., Rothe, M., and Brand, W. A.: Calcite-CO₂ mixed into CO₂-free air:
599 A new CO₂-in-air stable isotope reference material for the VPDB scale, *Rapid Commun.*
600 *Mass Spectrom.*, <https://doi.org/10.1002/rcm.1886>, 2005.
- 601 Ghosh, P., Adkins, J., Affek, H., Balta, B., Guo, W., Schauble, E. A., Schrag, D., and Eiler, J.
602 M.: ¹³C-¹⁸O bonds in carbonate minerals: A new kind of paleothermometer, *Geochim.*
603 *Cosmochim. Acta*, <https://doi.org/10.1016/j.gca.2005.11.014>, 2006.
- 604 Gopalakrishna, V. V. and Sastry, J. S.: Surface circulation over the shelf off the east coast of
605 India during the south west monsoon, *Indian J Mar Sci.*, 1985.
- 606 Goswami, B. B., Murtugudde, R., and An, S. II: Role of the Bay of Bengal warming in the
607 Indian summer monsoon rainfall trend, *Clim. Dyn.*, 59, 1733–1751,
608 <https://doi.org/10.1007/s00382-021-06068-1>, 2022.
- 609 Goswami, B. N.: A mechanism for the west-north-west movement of monsoon depressions,
610 *Nature*, 326, 376–378, <https://doi.org/10.1038/326376a0>, 1987.
- 611 Goswami, B. N., Krishnamurthy, V., and Anmalai, H.: A broad-scale circulation index for



- 612 the interannual variability of the Indian summer monsoon, *Q. J. R. Meteorol. Soc.*, 125, 611–
613 633, <https://doi.org/https://doi.org/10.1002/qj.49712555412>, 1999.
- 614 Govil, P. and Divakar Naidu, P.: Variations of Indian monsoon precipitation during the last
615 32kyr reflected in the surface hydrography of the Western Bay of Bengal, *Quat. Sci. Rev.*, 30,
616 3871–3879, <https://doi.org/10.1016/j.quascirev.2011.10.004>, 2011.
- 617 Gray, W. R. and Evans, D.: Nonthermal Influences on Mg/Ca in Planktonic Foraminifera: A
618 Review of Culture Studies and Application to the Last Glacial Maximum, *Paleoceanogr.*
619 *Paleoclimatology*, 34, 306–315, <https://doi.org/10.1029/2018PA003517>, 2019.
- 620 Guptha, M. V. S., Curry, W. B., Ittekkot, V., and Muralinath, A. S.: Seasonal variation in the
621 flux of planktic Foraminifera; sediment trap results from the Bay of Bengal, northern Indian
622 Ocean, *J. Foraminifer. Res.*, <https://doi.org/10.2113/gsjfr.27.1.5>, 1997.
- 623 Hönisch, B., Allen, K. A., Russell, A. D., Eggins, S. M., Bijma, J., Spero, H. J., Lea, D. W.,
624 and Yu, J.: Planktic foraminifers as recorders of seawater Ba/Ca, *Mar. Micropaleontol.*, 79,
625 52–57, <https://doi.org/10.1016/j.marmicro.2011.01.003>, 2011.
- 626 Horita, J. and Wesolowski, D. J.: Liquid-vapor fractionation of oxygen and hydrogen
627 isotopes of water from the freezing to the critical temperature, *Geochim. Cosmochim. Acta*,
628 58, 1–13, [https://doi.org/https://doi.org/10.1016/0016-7037\(94\)90096-5](https://doi.org/https://doi.org/10.1016/0016-7037(94)90096-5), 1994.
- 629 Huntington, K. W., Eiler, J. M., Affek, H. P., Guo, W., Bonifacie, M., Yeung, L. Y.,
630 Thiagarajan, N., Passey, B., Tripathi, A., Daëron, M., and Came, R.: Methods and limitations
631 of “clumped” CO₂ isotope ($\Delta 47$) analysis by gas-source isotope ratiomass spectrometry, *J.*
632 *Mass Spectrom.*, <https://doi.org/10.1002/jms.1614>, 2009.
- 633 Hurley, J. V. and Boos, W. R.: A global climatology of monsoon low-pressure systems, *Q. J.*
634 *R. Meteorol. Soc.*, 141, 1049–1064, <https://doi.org/10.1002/qj.2447>, 2015.



- 635 Jalihal, C., Srinivasan, J., and Chakraborty, A.: Modulation of Indian monsoon by water
636 vapor and cloud feedback over the past 22,000 years, *Nat. Commun.*, 10,
637 <https://doi.org/10.1038/s41467-019-13754-6>, 2019.
- 638 Jalihal, C., Srinivasan, J., and Chakraborty, A.: Different precipitation response over land and
639 ocean to orbital and greenhouse gas forcing, *Sci. Rep.*, 10, 1–11,
640 <https://doi.org/10.1038/s41598-020-68346-y>, 2020.
- 641 Jana, S., Gangopadhyay, A., and Chakraborty, A.: Impact of seasonal river input on the Bay
642 of Bengal simulation, *Cont. Shelf Res.*, <https://doi.org/10.1016/j.csr.2015.05.001>, 2015.
- 643 Jyothibabu, R., Arunpandi, N., Jagadeesan, L., Karnan, C., Lallu, K. R., and Vinayachandran,
644 P. N.: Response of phytoplankton to heavy cloud cover and turbidity in the northern Bay of
645 Bengal, *Sci. Rep.*, 8, 1–15, <https://doi.org/10.1038/s41598-018-29586-1>, 2018.
- 646 Kalnay, E., Kanamitsu, M., Kistler, R., Collins, W., Deaven, D., Gandin, L., Iredell, M.,
647 Saha, S., White, G., Woollen, J., Zhu, Y., Chelliah, M., Ebisuzaki, W., Higgins, W.,
648 Janowiak, J., Mo, K. C., Ropelewski, C., Wang, J., Leetmaa, A., Reynolds, R., Jenne, R., and
649 Joseph, D.: The NCEP/NCAR 40-year reanalysis project, *Bull. Amer. Meteor. Soc.*, 77, 437–
650 470, 1996.
- 651 Kiefer, D. A.: Chlorophyll a fluorescence in marine centric diatoms: Responses of
652 chloroplasts to light and nutrient stress, *Mar. Biol.*, 23, 39–46,
653 <https://doi.org/https://doi.org/10.1007/bf00394110>, 1973.
- 654 Kim, S. T. and O’Neil, J. R.: Equilibrium and nonequilibrium oxygen isotope effects in
655 synthetic carbonates, *Geochim. Cosmochim. Acta*, [https://doi.org/10.1016/S0016-7037\(97\)00169-5](https://doi.org/10.1016/S0016-7037(97)00169-5), 1997.
- 657 Kudrass, H. R., Hofmann, A., Doose, H., Emeis, K., and Ostseeforschung, I.: Modulation and



- 658 amplification of climatic changes in the Northern Hemisphere by the Indian summer
659 monsoon during the past 80 k . y, *Geology*, 29, 63–66,
660 [https://doi.org/https://doi.org/10.1130/0091-](https://doi.org/https://doi.org/10.1130/0091-7613(2001)029%3C0063:MAAOCC%3E2.0.CO;2)
661 [7613\(2001\)029%3C0063:MAAOCC%3E2.0.CO;2](https://doi.org/https://doi.org/10.1130/0091-7613(2001)029%3C0063:MAAOCC%3E2.0.CO;2), 2001.
- 662 Kuroyanagi, A. and Kawahata, H.: Vertical distribution of living planktonic foraminifera in
663 the seas around Japan, *Mar. Micropaleontol.*, 53, 173–196,
664 <https://doi.org/10.1016/j.marmicro.2004.06.001>, 2004.
- 665 Lakhani, K. Q., Lynch-Stieglitz, J., and Monteagudo, M. M.: Constraining calcification
666 habitat using oxygen isotope measurements in tropical planktonic foraminiferal tests from
667 surface sediments, *Mar. Micropaleontol.*, 170, 102074,
668 <https://doi.org/10.1016/j.marmicro.2021.102074>, 2022.
- 669 Lambeck, K., Rouby, H., Purcell, A., Sun, Y., and Sambridge, M.: Sea level and global ice
670 volumes from the Last Glacial Maximum to the Holocene, *Proc. Natl. Acad. Sci.*,
671 <https://doi.org/10.1073/pnas.1411762111>, 2014.
- 672 Liu, S., Zhang, H., Cao, P., Liu, M., Ye, W., Chen, M. Te, Li, J., Pan, H. J., Khokiattiwong,
673 S., Kornkanitnan, N., and Shi, X.: Paleoproductivity evolution in the northeastern Indian
674 Ocean since the last glacial maximum: Evidence from biogenic silica variations, *Deep. Res.*
675 *Part I Oceanogr. Res. Pap.*, 175, 103591, <https://doi.org/10.1016/j.dsr.2021.103591>, 2021.
- 676 Maeda, A., Kuroyanagi, A., Iguchi, A., Gaye, B., Rixen, T., Nishi, H., and Kawahata, H.:
677 Seasonal variation of fluxes of planktic foraminiferal tests collected by a time-series sediment
678 trap in the central Bay of Bengal during three different years, *Deep. Res. Part I Oceanogr.*
679 *Res. Pap.*, 183, 103718, <https://doi.org/10.1016/j.dsr.2022.103718>, 2022.
- 680 Masuda, Y., Yamanaka, Y., Smith, S. L., Hirata, T., Nakano, H., Oka, A., and Sumata, H.:
681 Photoacclimation by phytoplankton determines the distribution of global subsurface



- 682 chlorophyll maxima in the ocean, *Commun. Earth Environ.*, 2, 1–8,
683 <https://doi.org/10.1038/s43247-021-00201-y>, 2021.
- 684 Mehta, S., Singh, A., and Thirumalai, K.: Uncertainty in palaeosalinity estimates from
685 foraminiferal geochemical records in the northern Indian Ocean, *Palaeogeogr.*
686 *Palaeoclimatol. Palaeoecol.*, 569, 110326, <https://doi.org/10.1016/j.palaeo.2021.110326>,
687 2021.
- 688 Meinicke, N., Ho, S. L., Hannisdal, B., Nürnberg, D., Tripathi, A., Schiebel, R., and Meckler,
689 A. N.: A robust calibration of the clumped isotopes to temperature relationship for
690 foraminifers, *Geochim. Cosmochim. Acta*, 270, 160–183,
691 <https://doi.org/10.1016/j.gca.2019.11.022>, 2020.
- 692 Merlivat, L. and Jouzel, J.: Global climatic interpretation of the deuterium-oxygen 18
693 relationship for precipitation, *J. Geophys. Res. Ocean.*, 84, 5029–5033,
694 <https://doi.org/https://doi.org/10.1029/JC084iC08p05029>, 1979.
- 695 Mulitza, S., Boltovskoy, D., Donner, B., Meggers, H., Paul, A., and Wefer, G.: Temperature:
696 $\delta^{18}\text{O}$ relationships of planktonic foraminifera collected from surface waters, *Palaeogeogr.*
697 *Palaeoclimatol. Palaeoecol.*, [https://doi.org/10.1016/S0031-0182\(03\)00633-3](https://doi.org/10.1016/S0031-0182(03)00633-3), 2003.
- 698 Müller, P. J., Kirst, G., Ruhland, G., Von Storch, I., and Rosell-Melé, A.: Calibration of the
699 alkenone paleotemperature index U37K based on core-tops from the eastern South Atlantic
700 and the global ocean (60°N–60°S), *Geochim. Cosmochim. Acta*, 62, 1757–1772,
701 [https://doi.org/10.1016/S0016-7037\(98\)00097-0](https://doi.org/10.1016/S0016-7037(98)00097-0), 1998.
- 702 Munir, S., Sun, J., Morton, S. L., Zhang, X., and Ding, C.: Horizontal Distribution and
703 Carbon Biomass of Planktonic Foraminifera in the Eastern Indian Ocean, 14, 1–15,
704 <https://doi.org/10.3390/w14132048>, 2022.



- 705 Parthasarathy, B., Munot, A. A., and Kothawale, D. R.: All-India monthly and seasonal
706 rainfall series: 1871-1993, *Theor. Appl. Climatol.*, 49, 217–224,
707 <https://doi.org/10.1007/BF00867461>, 1994.
- 708 Peral, M., Daëron, M., Blamart, D., Bassinot, F., Dewilde, F., Smialkowski, N., Isguder, G.,
709 Bonnin, J., Jorissen, F., Kissel, C., Michel, E., Vázquez Riveiros, N., and Waelbroeck, C.:
710 Updated calibration of the clumped isotope thermometer in planktonic and benthic
711 foraminifera, *Geochim. Cosmochim. Acta*, <https://doi.org/10.1016/j.gca.2018.07.016>, 2018.
- 712 Pourmand, A., Marcantonio, F., and Schulz, H.: Variations in productivity and eolian fluxes
713 in the northeastern Arabian Sea during the past 110 ka, *Earth Planet. Sci. Lett.*, 221, 39–54,
714 [https://doi.org/10.1016/S0012-821X\(04\)00109-8](https://doi.org/10.1016/S0012-821X(04)00109-8), 2004.
- 715 Prell, W. L. and Curry, W. B.: Faunal and isotopic indices of monsoonal upwelling-western
716 arabian sea., *Oceanol. acta*, 4, 91–98, 1981.
- 717 Quamar, M. F. and Bera, S. K.: Pollen records of vegetation dynamics, climate change and
718 ISM variability since the LGM from Chhattisgarh State, central India, *Rev. Palaeobot.*
719 *Palynol.*, 278, 104237, <https://doi.org/10.1016/j.revpalbo.2020.104237>, 2020.
- 720 Rajeev, S., Rajiv, N., Andreas, M., and Syee, W.: Linkage between seasonal insolation
721 gradient in the tropical northern hemisphere and the sea surface salinity of the equatorial
722 Indian Ocean during the last glacial period, *Acta Geol. Sin. (English Ed.)*, 86, 1265–1275,
723 <https://doi.org/10.1111/j.1755-6724.2012.00746.x>, 2012.
- 724 Rashid, H., England, E., Thompson, L., and Polyak, L.: Late glacial to holocene indian
725 summer monsoon variability based upon sediment records taken from the bay of Bengal,
726 *Terr. Atmos. Ocean. Sci.*, [https://doi.org/10.3319/TAO.2010.09.17.02\(TibXS\)](https://doi.org/10.3319/TAO.2010.09.17.02(TibXS)), 2011.
- 727 Raza, T., Ahmad, S. M., Steinke, S., Raza, W., Lone, M. A., Beja, S. K., and Suseela, G.:



- 728 Glacial to Holocene changes in sea surface temperature and seawater $\delta^{18}\text{O}$ in the northern
729 Indian Ocean, *Palaeogeogr. Palaeoclimatol. Palaeoecol.*, 485, 697–705,
730 <https://doi.org/10.1016/j.palaeo.2017.07.026>, 2017.
- 731 Reagan, J. R., Boyer, T. P., García, H. E., Locarnini, R. A., Baranova, O. K., Bouchard, C.,
732 Cross, S. L., Mishonov, A. V., Paver, C. R., Seidov, D., Wang, Z., and Dukhovskoy, D.:
733 World Ocean Atlas 2023., NOAA Natl. Centers Environ.
734 Information.<https://www.ncei.noaa.gov/archive/accession/0270533>. Accessed [25/04/2024],
735 2024.
- 736 Reimer, P. J., Bard, E., Bayliss, A., Beck, J. W., Blackwell, P. G., Ramsey, C. B., Buck, C.
737 E., Cheng, H., Edwards, R. L., Friedrich, M., Grootes, P. M., Guilderson, T. P., Haflidason,
738 H., Hajdas, I., Hatté, C., Heaton, T. J., Hoffmann, D. L., Hogg, A. G., Hughen, K. A., Kaiser,
739 K. F., Kromer, B., Manning, S. W., Niu, M., Reimer, R. W., Richards, D. A., Scott, E. M.,
740 Southon, J. R., Staff, R. A., Turney, C. S. M., and van der Plicht, J.: IntCal13 and Marine13
741 Radiocarbon Age Calibration Curves 0–50,000 Years cal BP, *Radiocarbon*,
742 https://doi.org/10.2458/azu_js_rc.55.16947, 2013.
- 743 Rommerskirchen, F., Condon, T., Mollenhauer, G., Dupont, L., and Schefuss, E.: Miocene to
744 Pliocene development of surface and subsurface temperatures in the Benguela Current
745 system, *Paleoceanography*, 26, 1–15, <https://doi.org/10.1029/2010PA002074>, 2011.
- 746 Sachse, D., Billault, I., Bowen, G. J., Chikaraishi, Y., Dawson, T. E., Feakins, S. J., Freeman,
747 K. H., Magill, C. R., McInerney, F. A., Van Der Meer, M. T. J., Polissar, P., Robins, R. J.,
748 Sachs, J. P., Schmidt, H. L., Sessions, A. L., White, J. W. C., West, J. B., and Kahmen, A.:
749 Molecular paleohydrology: Interpreting the hydrogen-isotopic composition of lipid
750 biomarkers from photosynthesizing organisms, *Annu. Rev. Earth Planet. Sci.*, 40, 221–249,
751 <https://doi.org/10.1146/annurev-earth-042711-105535>, 2012.



- 752 Samanta, D., Hameed, S. N., Jin, D., Thilakan, V., Ganai, M., Rao, S. A., and Deshpande,
753 M.: Impact of a Narrow Coastal Bay of Bengal Sea Surface Temperature Front on an Indian
754 Summer Monsoon Simulation, *Sci. Rep.*, 8, 1–12, [https://doi.org/10.1038/s41598-018-35735-](https://doi.org/10.1038/s41598-018-35735-3)
755 3, 2018.
- 756 Saxena, H. and Pandey, V. K.: Investigation of Indian Summer Monsoon Rainfall
757 Relationship with the Bay of Bengal Sea Surface Temperature and Currents, in: *Recent*
758 *Technologies for Disaster Management and Risk Reduction, Earth and Environmental*
759 *Sciences Library*. Springer, Cham., [https://doi.org/https://doi.org/10.1007/978-3-030-76116-](https://doi.org/https://doi.org/10.1007/978-3-030-76116-5_12)
760 5_12, 2021.
- 761 Schneider, D. P., Deser, C., J. Fasullo, and Trenberth, K. E.: Climate Data Guide Spurs
762 Discovery and Understanding., *Eos Trans. AGU*, 94, 121–122,
763 <https://doi.org/https://doi.org/10.1002/2013eo130001>, 2013.
- 764 Sein, D. V., Martyanov, S. D., Dvornikov, A. Y., Cabos, W., Ryabchenko, V. A., Mishra, A.
765 K., Limareva, N., Alekseeva, E., Jacob, D., and Kumar, P.: Future climate change in the
766 Northern Indian Ocean as simulated with a high-resolution regional earth system model,
767 *Clim. Dyn.*, 62, 911–932, <https://doi.org/10.1007/s00382-023-06939-9>, 2024.
- 768 Sharma, S., Ha, K. J., Yamaguchi, R., Rodgers, K. B., Timmermann, A., and Chung, E. S.:
769 Future Indian Ocean warming patterns, *Nat. Commun.*, 14, [https://doi.org/10.1038/s41467-](https://doi.org/10.1038/s41467-023-37435-7)
770 023-37435-7, 2023.
- 771 Shenoi, S. S. C.: Differences in heat budgets of the near-surface Arabian Sea and Bay of
772 Bengal: Implications for the summer monsoon, *J. Geophys. Res.*, 107, 3052,
773 <https://doi.org/10.1029/2000JC000679>, 2002.
- 774 Shetye, S. R., Shenoi, S. S. C., Gouveia, A. D., Michael, G. S., Sundar, D., and Nampoothiri,
775 G.: Wind-driven coastal upwelling along the western boundary of the Bay of Bengal during



- 776 the southwest monsoon, *Cont. Shelf Res.*, 11, 1397–1408,
777 [https://doi.org/https://doi.org/10.1016/0278-4343\(91\)90042-5](https://doi.org/https://doi.org/10.1016/0278-4343(91)90042-5), 1991.
- 778 Singh, A., Mohiuddin, A., Ramesh, R., and Raghav, S.: Estimating the Loss of Himalayan
779 Glaciers under Global Warming Using the δ 18 O-Salinity Relation in the Bay of Bengal,
780 *Environ. Sci. Technol. Lett.*, 1, 249–253, <https://doi.org/10.1021/ez500076z>, 2014.
- 781 Sonzogni, C., Bard, E., and Rostek, F.: Tropical sea-surface temperatures during the last
782 glacial period: A view based on alkenones in Indian Ocean sediments, *Quat. Sci. Rev.*, 17,
783 1185–1201, [https://doi.org/10.1016/S0277-3791\(97\)00099-1](https://doi.org/10.1016/S0277-3791(97)00099-1), 1998.
- 784 Stuiver, M. and Reimer, P. J.: CALIB rev. 8, *Radiocarbon*, 35, 215–230, 1993.
- 785 Tapia, R., Ho, S. L., Wang, H. Y., Groeneveld, J., and Mohtadi, M.: Contrasting vertical
786 distributions of recent planktic foraminifera off Indonesia during the southeast monsoon:
787 implications for paleoceanographic reconstructions, 19, 3185–3208,
788 <https://doi.org/10.5194/bg-19-3185-2022>, 2022.
- 789 Tierney, J. E., Zhu, J., King, J., Malevich, S. B., Hakim, G. J., and Poulsen, C. J.: Glacial
790 cooling and climate sensitivity revisited, *Nature*, 584, 569–573,
791 <https://doi.org/10.1038/s41586-020-2617-x>, 2020.
- 792 Trenberth, K. and Fasullo, J.: "The Climate Data Guide: ERA-Interim: derived components."
793 Retrieved from [https://climatedataguide.ucar.edu/climate-data/era-interim-derived-](https://climatedataguide.ucar.edu/climate-data/era-interim-derived-components)
794 components on 2024-03-30., *Natl. Cent. Atmos. Res. Staff (Eds)*. Last Modif. 2022-11-07,
795 2022.
- 796 Tripathi, A. K., Eagle, R. A., Thiagarajan, N., Gagnon, A. C., Bauch, H., Halloran, P. R., and
797 Eiler, J. M.: ^{13}C - ^{18}O isotope signatures and "clumped isotope" thermometry in foraminifera
798 and coccoliths, *Geochim. Cosmochim. Acta*, 74, 5697–5717,



799 <https://doi.org/10.1016/j.gca.2010.07.006>, 2010.

800 Vecchi, G. A. and Harrison, D. E.: Monsoon Breaks and Subseasonal Sea Surface

801 Temperature Variability in the Bay of Bengal, *J. Clim.*, 15, 1485–1493,

802 <https://doi.org/https://doi.org/10.1175/1520->

803 0442(2002)015%3C1485:MBASSS%3E2.0.CO;2, 2002.

804 Verma, K., Singh, A. D., Singh, P., Singh, H., Satpathy, R. K., Uddandam, P. R., and Naidu,

805 P. D.: Monsoon-related changes in surface hydrography and productivity in the Bay of

806 Bengal over the last 45 kyr BP, *Palaeogeogr. Palaeoclimatol. Palaeoecol.*, 589, 110844,

807 <https://doi.org/10.1016/j.palaeo.2022.110844>, 2022.

808 Wang, P. X., Wang, B., Cheng, H., Fasullo, J., Guo, Z. T., Kiefer, T., and Liu, Z. Y.: The

809 global monsoon across time scales: Mechanisms and outstanding issues, *Earth-Science Rev.*,

810 174, 84–121, <https://doi.org/10.1016/j.earscirev.2017.07.006>, 2017.

811 Wang, Y. V., Larsen, T., Lauterbach, S., Andersen, N., Blanz, T., Krebs-Kanzow, U., Gierz,

812 P., and Schneider, R. R.: Higher sea surface temperature in the Indian Ocean during the Last

813 Interglacial weakened the South Asian monsoon, *Proc. Natl. Acad. Sci. U. S. A.*, 119,

814 <https://doi.org/10.1073/pnas.2107720119>, 2022.

815 Webster, P. J.: The role of hydrological processes in ocean-atmosphere interactions, *Rev.*

816 *Geophys.*, 32, 427–476, <https://doi.org/10.1029/94RG01873>, 1994.

817 Weldeab, S., Rühlemann, C., Ding, Q., Khon, V., Schneider, B., and Gray, W. R.: Impact of

818 Indian Ocean surface temperature gradient reversals on the Indian Summer Monsoon, *Earth*

819 *Planet. Sci. Lett.*, 578, 117327, <https://doi.org/10.1016/j.epsl.2021.117327>, 2022.

820 Wuchter, C., Schouten, S., Wakeham, S. G., and Damsté, J. S. S.: Archaeal tetraether

821 membrane lipid fluxes in the northeastern Pacific and the Arabian Sea: Implications for



- 822 TEX86 paleothermometry, *Paleoceanography*, 21, 1–9,
823 <https://doi.org/10.1029/2006PA001279>, 2006.
- 824 Yoon, J. H. and Chen, T. C.: Water vapor budget of the Indian monsoon depression, *Tellus*,
825 *Ser. A Dyn. Meteorol. Oceanogr.*, 57, 770–782, [https://doi.org/10.1111/j.1600-](https://doi.org/10.1111/j.1600-0870.2005.00145.x)
826 [0870.2005.00145.x](https://doi.org/10.1111/j.1600-0870.2005.00145.x), 2005.
- 827 Zaarur, S., Affek, H. P., and Brandon, M. T.: A revised calibration of the clumped isotope
828 thermometer, *Earth Planet. Sci. Lett.*, <https://doi.org/10.1016/j.epsl.2013.07.026>, 2013.
- 829